Wave-equation migration with dithered plane waves

Francesco Perrone & Paul Sava
Center for Wave Phenmena, Colorado School of Mines

ABSTRACT
Wave-equation based shot-record migration provides accurate images but is computationally expensive because every shot must be migrated separately. Shot-encoding migration, such as random shot-encoding or plane-wave migration, aims to reduce the computational cost of the imaging process by combining the original data into synthetic experiments. Random shot-encoding migration and plane-wave migration have different and complementary features: the first recovers the full spatial bandwidth of the image but introduces strong artifacts, which are due to the interference between different shot wavefields; the second provides an image with limited spatial detail but free of crosstalk noise. We design a hybrid scheme that combines linear and random shot-encoding in order to counterbalance the drawbacks and merge the advantages of these two techniques. We advocate mixed shot-encoding migration through dithering of plane waves, which increases the spatial bandwidth relative to conventional plane-wave migration and reduces crosstalk noise relative to random shot-encoding migration. Migration with dithered plane waves operates as a hybrid encoding scheme in-between the end members represented by plane-wave migration and random shot-encoding. The combination of complementary encodings is effective in reducing the trade-off between spatial resolution and crosstalk noise; nonetheless, the noise cannot be completely removed. We test two denoising algorithms for eliminating the residual noise in the encoded image. We conclude that because crosstalk noise has spectral properties similar to the signal, denoising techniques in the image domain are less effective than our mixed encoding scheme. In particular in poorly illuminated areas, better encoding is a more effective solution for controlling crosstalk and recovering a correct image. Migration with dithered plane waves has several advantages: every synthetic experiment images in a larger aperture with respect to shot-record migration; crosstalk noise is controlled relative to random shot-encoding; and higher spatial resolution is achievable with regard to linear shot-encoding. Computational cost is also reduced relative to both random and linear shot-encoding migration since fewer synthetic experiments are necessary for obtaining high signal-to-noise ratio and high spatial resolution in the final image.

Key words: imaging, migration, shot-encoding

1 INTRODUCTION

In conventional seismic depth-imaging, data are acquired by means of independent experiments that are then separately imaged. In wave-equation migration, the imaging procedure consists of two steps: wavefield extrapolation, from data recorded on the surface to all locations in the subsurface, and the application of an imaging condition (Claerbout, 1985). The extrapolation step is linear but computationally intensive; the imaging step is relatively cheap from the computational point of view but nonlinear. The imaging condition extracts an image where the data, extrapolated backward in time, match the source wavefield, extrapolated forward in time. A conventional imaging condition evaluates the matching between the source and receiver wavefields through their crosscorrelation (Claerbout, 1985).

In shot-record (shot-profile) migration, every experiment is imaged separately and the total cost is therefore a linear function of the number of experiments. Moreover, the more accurate the wavefield extrapolation scheme, the higher its com-

putational cost. In the case of reverse-time migration (RTM) (Baysal et al., 1983), the computational cost is high, thus posing a challenge for industrial applications. Simultaneous shot migration has several benefits: first, we can reduce the overall time of the migration procedure, thus reducing the cost; second, we can exploit the possibility of imaging in a fixed time and in a bigger aperture with respect to shot-profile migration in the migration velocity analysis loop, which is a crucial step in the seismic inversion process.

Random shot-encoding migration (Morton & Ober, 1998; Romero et al., 2000) is used to image data by simultaneously migrating a number of shots, which are linearly combined after the application of random delays. The main goal is to reduce the computational cost of wave-equation migration. The drawback is that unrelated shots interfere with one another, thus leading to artifacts commonly referred to as crosstalk. For random shot-encoding, the power of the artifacts in the image decreases as $1/M$ with M being the number of encodings considered, i.e., the number of stacked encoded images.

An intrinsic problem in shot-profile migration is that the natural pre-stack gather (the shot indexed gather) cannot be directly or easily related to the incidence angle or other illumination-related quantities (Soubaras, 2006). To overcome this difficulty, several authors propose synthesizing composite shots by applying delays that are linear functions in the original shot positions (Whitmore, 1995; Zhang et al., 2005; Liu et al., 2006). These new synthetic shots are synthetic plane-waves and the new data are, therefore, the response of the subsurface to an incident plane-wave. The natural pre-stack index for these experiments is the ray parameter $p = sin(\alpha)/v$, where α is the take-off angle of the synthetic plane-wave. This index is a surface-related parameter and does not remove the complexity of the overburden at the image point, i.e., it does not represent the illumination of the image point as a function of the angle of incidence.

The angle of incidence represents a preferential domain for indexing seismic images. Stolk & de Hoop (2001) show that wave-equation common-angle image gathers are not affected by multipathing artifacts that characterize kirchhoff migration (Stolk & Symes, 2004); hence, they represent a powerful tool for performing velocity analysis via semblance principle. The plane-wave take-off angle is directly related to the angle of incidence in depth only if the velocity model is layered and laterally homogeneous; in complex velocity models, the angle of incidence can be computed by considering extended images and transforming them into the angle domain (Rickett & Sava, 2002; Sava & Fomel, 2003).

Plane-wave migration, or linear-shot encoding migration (L-SEM), is equivalent to shot-profile migration when one considers all plane waves that describe the data. Zhang et al. (2005) present an equation for the minimum number of plane-wave components necessary for correctly representing the data in a certain range of take-off angles. Soubaras (2006) presents a different strategy that exploits a unitary transformation for combining the original shots. Modulated-shot encoding produces an image equivalent to shot-profile migration as well as image-gathers indexed by ray parameter p, but it is less costly than plane-wave migration. Modulated shot-encoding and plane-wave migration are closely related: both combine the shots through a unitary transformation, but while modulated shot-encoding uses a frequency *independent* unitary transformation, plane-wave migration uses a frequency *dependent* basis. They span the same space frequency-wavenumber $(\omega, \mathbf{p})$, but in different ways. The modulated-shot encoding algorithm represents an improvement over both plane-wave migration and shot-record migration, and the computational gain is preserved in the time-domain implementation (Zhang et al., 2007). In this work, we present an alternative algorithm, suitable for reverse-time migration, which allows straightforward implementation, quality control of the final image, and computational cost reduction.

The artifacts produced in simultaneous migration of different shots originate in the migration operator. The migration operator (wavefield extrapolation followed by the application of an imaging condition) is simply the adjoint of the forward Born operator used for modeling the data (Lailly, 1983) which is "almost" a unitary operator for a single shot-profile experiment. For simultaneous shot migration, the migration operator is no longer unitary and this is evidenced by the artifacts that contaminate the image. An alternative approach to this problem is least-squares migration; in this way we can compensate for the non-unitary nature of the migration operator and eliminate the artifacts in the image (Tang & Biondi, 2009). Least-squares migration is effective but computationally expensive: shot-encoding is intended to reduce the computational cost but a least-squares inversion of such a large linear problem makes the process less cost-effective. It is interesting to observe the similarities between the least-squares approach to simultaneous shot migration and processing of blended data (Berkhout, 2008), where datasets with overlapping shots are processed and imaged in a least-square sense (Verschuur & Berkhout, 2009; Berkhout et al., 2009).

In this paper, we analyze shot-encoding schemes, namely random-shot encoding (R-SEM) (Romero et al., 2000) and plane-wave migration (Zhang et al., 2005), that are suitable for reverse-time migration. We look at the behavior of the two methods with respect to crosstalk artifacts and spatial resolution in the final image. Our goal is to develop an improvement over random shot-encoding that converges faster to the shot-record migration (SRM) result and that controls the artifacts introduced in the image by the interference of different experiments. At the same time, we want to achieve higher spatial resolution with respect to plane-wave migration, which trades speed for spatial resolution by using only certain plane-wave components for reconstructing the image of the subsurface. Moreover, imaging plane-wave components with a high take-off angle (or ray parameter $\mathbf{p}$), when a time-domain finite difference scheme is used (like in RTM), requires an increase in the computational time and cost since long delays have to be taken into account. From this analysis, we design a hybrid encoding scheme that combines L-SEM and R-SEM. First, we construct the linear delay function that produces the synthetic plane-wave response from the original data; then, we dither the planar wavefront with random delays in order to increase the

spatial resolution without migrating additional plane waves. We test it on the synthetic Sigsbee model and show that it is more effective than both L-SEM and R-SEM. In areas with poor or uneven illumination, the hybrid approach recovers the full spatial bandwidth of the image, in contrast to L-SEM, and is less prone to crosstalk noise than R-SEM.

2 SHOT-ENCODING METHODS

The imaging condition is a nonlinear operation; it is not able to distinguish between wavefields from different shots and produces artifacts when several experiments are simultaneously migrated. Let us consider the source wavefields $s_i(\mathbf{x},t)$ and the receiver wavefields $r_i(\mathbf{x},t)$, where the index i indicates the shot number. We can combine wavefields of different shots and extrapolate them all at once because the wave equation we use is linear in the wavefield; however, problems arise in the extraction of the image. Conventional imaging condition involves computing the time crosscorrelation at every location $\mathbf{x}$ in space of the source and receiver wavefields $S(\mathbf{x},t)$ and $R(\mathbf{x},t)$ and stacking over time:

$$I(\mathbf{x}) = \sum_t S(\mathbf{x},t)R(\mathbf{x},t). \tag{1}$$

If the wavefields $S(\mathbf{x},t)$ and $R(\mathbf{x},t)$ are, respectively, the combination of all shot source and receiver wavefields with different delays, then we obtain:

$$\begin{aligned} I(\mathbf{x}) &= \sum_t \sum_i \sum_k s_i(\mathbf{x},t-\tau_i) r_k(\mathbf{x},t-\tau_k) \\ &= \sum_i I_i(\mathbf{x}) + \sum_t \sum_{l\neq k} s_l(\mathbf{x},t-\tau_l) r_k(\mathbf{x},t-\tau_k), \end{aligned}$$

where $I_i(\mathbf{x})$ is the image obtained from the ith shot, and the term $\sum_t \sum_{l\neq k} s_l(\mathbf{x},t-\tau_l) r_k(\mathbf{x},t-\tau_k)$ represents the crosstalk artifacts produced by the imaging condition as result of the simultaneous migration of different experiments. Shot-encoding migration deals with the design of an optimal combination of the original data that allows one to simultaneously migrate several shots at once, control the crosstalk noise, and recover the correct image of the structure that generated the recorded data.

Different encoding schemes have been discussed in the literature. Random shot-encoding (R-SEM) (Romero et al., 2000) and linear shot-encoding (L-SEM) (Zhang et al., 2005) apply simple delays to the source and receiver wavefields of every shot. In random shot-encoding, a random delay is applied to each one of the shot wavefields prior to the composition of the synthetic experiments. The uncorrelation of the delays is reflected in uncorrelated artifacts that can be stacked out by summing up the images obtained from different realizations of random delays.

On the other hand, linear shot-encoding aims to construct the response of the Earth to synthetic plane waves by applying delays that are linear functions of the shot positions. Linear shot-encoding migration has been proven to be equivalent to shot-record migration if a sufficient number of plane-waves is considered. Random shot-encoding is equivalent to shot-record migration when considering an infinite number of realizations of random delays. For both methods, because of the model-dependence of the problem, the question of how many encodings we *really* need for obtaining a correct image is still open (Stork & Kapoor, 2004; Etgen, 2005) . For example, for imaging a single horizontal reflector, we need a single plane wave; on the other hand, for highly heterogeneous media and complex structures, a more complete illumination of the spatial wavenumber domain is required. In the latter case, random shot-encoding can represent a more economic solution, given the acceptable level of crosstalk.

A third encoding scheme that involves more than just simple delays is modulated-shot encoding (Soubaras, 2006) or, in the time-domain implementation, harmonic-source encoding (Zhang et al., 2007). These strategies are effective but not straightforward to implement, especially the time-domain implementation. Harmonic-source encoding involves the convolution of the original data with a filter that decays like $1/t$, and particular care is needed in the choice of the encoding parameters. Nonetheless, both methods halve the computational cost of a typical production project (Soubaras, 2006; Zhang et al., 2007).

Our work aims to find a simple and economic way to image a survey using RTM. We focus on random and linear shot-encoding migration, and all considerations are drawn from these two references and their features with respect to the standard shot-profile migration.

Both random and linear shot-encoding can be described using a general formulation of the encoding procedure. In fact, we can express the synthetic wavefields as a weighted sum of the actual shot wavefields appropriately delayed:

$$S(\mathbf{x},t,\theta) = \sum_k s_k(\mathbf{x},t) * \delta(t - f(\mathbf{x}_k,\theta)) \tag{2}$$

and

$$R(\mathbf{x},t,\theta) = \sum_l r_l(\mathbf{x},t) * \delta(t - f(\mathbf{x}_l,\theta)), \tag{3}$$

where $f(\mathbf{x}_k,\theta)$ represents the delay applied to the kth shot wavefields as a function of the shot position $\mathbf{x}_k$ and the parameter θ. The parameter θ spans the encoding axis. For example, in the case of plane-wave migration in a 2D model (Whitmore, 1995; Zhang et al., 2005), $f(x_k,\theta) = \frac{\sin(\alpha\theta)}{v}(x_k - x_0)$, where x_0 is a reference point and $\alpha\theta$ represents the take-off angle of a single plane wave; for random shot-encoding, $f(\mathbf{x}_k,\theta)$ is a random process with different values for every shot position $\mathbf{x}_k$, where the parameter θ indexes the random delay realizations.

If N represents the total number of shots and M the number of different encodings (plane-waves or random delay realizations), the strategy is effective if $M \ll N$, i.e., if we can obtain an image which is comparable in quality to shot-record migration with a smaller number of migrations.

The wave-equation used in seismic imaging is linear in the wavefield; hence, we can linearly combine wavefields of

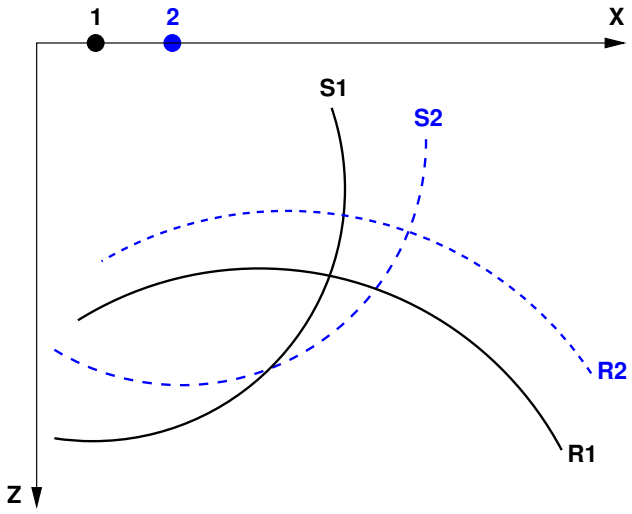


Figure 1. Artifacts generated by the imaging condition: the wavefields corresponding to different shots are represented with different colors ad different lines and indicated with numbers 1 and 2. The source wavefields are S1 and S2, the receiver wavefields R1 and R2. The correct image is produced where the wavefields of the same shots coincide, i.e., where the two solid lines, S1 and R1, and the two dashed lines, S2 and R2, intersect. Shot-encoding migration generates artifacts where S1 intersects R2 and S2 intersects R1.

different shots and numerically propagate their superposition in the subsurface model. However, the imaging condition is a nonlinear operation and introduces crosstalk between different experiments. The cartoon in Figure 1 describes the mechanism that produces crosstalk when two shots are simultaneously migrated. When the source and receiver wavefields belonging to different experiments match in time, the imaging condition extracts an image which does not correspond with a reflection.

If we substitute the expressions for the synthetic wavefields, equation 2 and equation 3, into the imaging condition in equation 1 and then transform in the frequency domain, we obtain

$$I(\mathbf{x}) = \sum_{\omega} \sum_{k} \sum_{l} s_k(\mathbf{x},\omega) r_l^*(\mathbf{x},\omega) W_{kl}, \qquad (4)$$

where

$$W_{kl} = \sum_{\theta} e^{i\omega[f(\mathbf{x}_l,\theta) - f(\mathbf{x}_k,\theta)]}. \qquad (5)$$

The matrix W_{kl}, which has the shot positions $\mathbf{x}_l$ and $\mathbf{x}_k$ as rows and columns, represents the coupling between different shots in equation 4 and it is fully determined by the encoding function $f(\cdot,\cdot)$.

An encoding scheme is considered equivalent to shot-record migration if the crosstalk term in equation 4 approximates the identity matrix, i.e., if the following condition is satisfied:

$$W_{kl} = \sum_{\theta} e^{i\omega[f(\mathbf{x}_l,\theta) - f(\mathbf{x}_k,\theta)]} \approx \delta_{kl}, \qquad (6)$$

where δ_{kl} is the Kronecker symbol.

In the following sections, we study the crosstalk term for linear shot-encoding and random shot-encoding. We highlight the main features in terms of spatial bandwidth achievable in the final image and crosstalk noise, and then we design a strategy for combining the advantages and controlling the drawbacks of these two schemes. We recognize linear shot-encoding and random shot-encoding as end members of a more general family of encodings, which we can span by controlling the correlation of the delays of neighboring shots. Figure 2 describes our idea; fixing the computational cost, we can move from plane-wave migration to random shot-encoding, i.e., from low crosstalk and low spatial bandwidth to high crosstalk and high spatial resolution in the final image. The correlation of the delays of neighboring shots involves a tuning parameter that controls the dithering of an initial plane-wave. In Figures 3(a)-3(c), we respectively show the source wavefield for linear shot-encoding, random shot-encoding and a combination of the two, in which the initial plane wave is dithered by a random perturbation. In the following, we analyze L-SEM and R-SEM and introduce mixed shot-encoding migration (M-SEM) as their combination.

2. 1 Linear shot-encoding migration

In linear shot-encoding, the recorded wavefields of different experiments are combined in order to obtain the response to a synthetic plane wave. The encoding function is linear in the shot position and depends on one parameter, which represents the ray parameter $\mathbf{p}_\theta$ associated with a particular plane wave:

$$f(\mathbf{x}_k,\theta) = \mathbf{p}_\theta \cdot (\mathbf{x}_k - \mathbf{x}_0), \qquad (7)$$

where $\mathbf{x}_0$ represents an arbitrary reference point.

Let us assume that $\mathbf{p}_\theta$ is a continuous parameter; if the expression in equation 7 is substituted into the expression de-

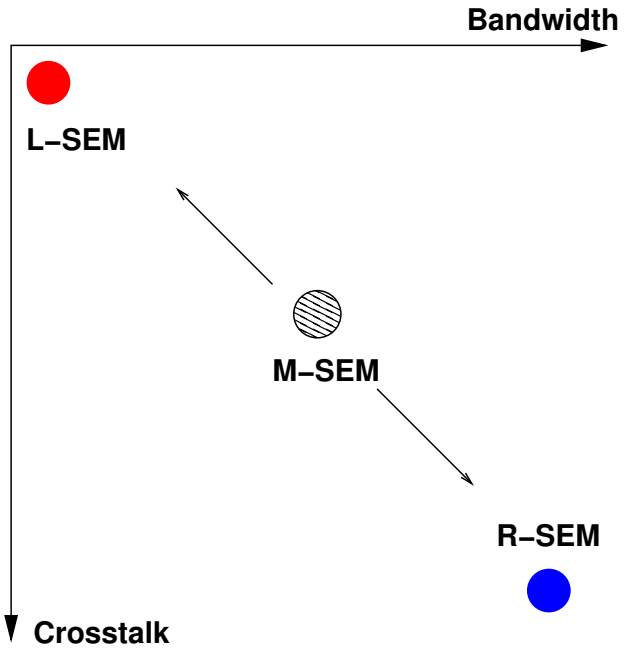


Figure 2. Trade-off between bandwidth and crosstalk for different shot-encoding schemes. L-SEM achieves a clean image with low spatial resolution, while R-SEM obtains a full bandwidth image highly contaminated by crosstalk noise. For drawing the cartoon, we assume fixed computational cost.

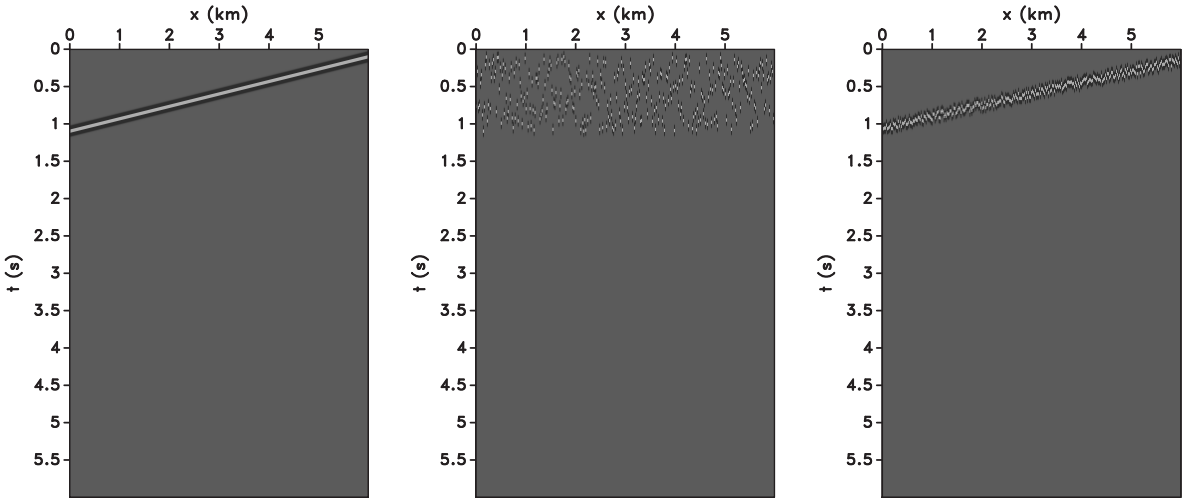


Figure 3. Examples of source wavefield for (a) L-SEM, (b) R-SEM, and (c) M-SEM. Mixed shot-encoding consists in dithering the wavefront we synthesize for L-SEM.

scribing the crosstalk, we obtain

$$W_{kl} = \int e^{i\omega \mathbf{p}_\theta \cdot (\mathbf{x}_k - \mathbf{x}_l)} d\mathbf{p}_\theta. \quad (8)$$

The expression in equation 8 is actually proportional to the Dirac delta $\delta(\mathbf{x}_k - \mathbf{x}_l)$; this means that plane-wave migration is equivalent to shot-record migration if we consider all ray parameters that reconstruct the data. In the real world, we sample the $\mathbf{p}$-space and then we have only a discretized version of the integral in equation 8:

$$W_{kl} = \sum_\theta e^{i\omega \mathbf{p}_\theta \cdot (\mathbf{x}_k - \mathbf{x}_l)}. \quad (9)$$

Several papers discuss the sampling requirements for the $\mathbf{p}$-space (Zhang et al., 2005; Stork & Kapoor, 2004; Etgen, 2005); the take-off angle range constrains the minimum number of plane waves necessary for correctly reconstructing the data in that range. At the same time, the angle range defines the computational cost for RTM and the accuracy of the image reconstruction; reducing the angle range decreases not only the computational cost but also the quality of the final image. If we assume that the ray parameter space is properly sampled and the synthesized plane waves are not aliased, then equation 9 represents a *sinc* function (the DFT of a discrete boxcar function) and tends to a delta function if we increase the take-off angle range.

We can display the crosstalk matrix for a given number of plane waves and analyze the behavior as a function of the number of $\mathbf{p}$ components considered. In Figures 4, we observe how the crosstalk term becomes spikier by imaging more plane-wave components. This is because, for linear shot-encoding, the crosstalk term is actually an approximate representation of the identity operator (equations 8-9).

2. 2 Random shot-encoding migration

In random shot-encoding, the delay of every shot is drawn from a random process and the parameter θ is the realization index. We use the following notation:

$$f(\mathbf{x}_k, \theta) \sim t_{max} \mathcal{U}; \quad (10)$$

at every shot location $\mathbf{x}_k$, the delay $f(\mathbf{x}_k, \theta)$ is a random variable uniformly distributed between 0 and t_{max}; $\mathcal{U}$ represents the uniform distribution between 0 and 1. If we indicate with t_k^θ the delay for the kth shot in the θth synthetic experiment, we can write the crosstalk matrix as

$$W_{kl} = \sum_\theta e^{i\omega[t_l^\theta - t_k^\theta]} = M\delta_{kl} + (1 - \delta_{kl}) \sum_\theta e^{i\omega[t_l^\theta - t_k^\theta]}. \quad (11)$$

Equation 11 shows that the crosstalk depends on the relative delay difference between different shots. The delay difference changes the spatial location of the artifacts in the image for different realizations of random delays. On the other hand, the correct structural image is always obtained at the correct location. Since the delays are random independent variables, the location of the artifacts will be an independent variable as well. The random superposition of the artifacts in space and the null DC component of the wavelet of the recorded signal partially stack out the crosstalk noise; the subsequent stack over different random delay realizations further improves the signal-to-noise ratio, since the positions of the reflectors do not depend on the encoding delays and their contribution will always stack constructively (Romero et al., 2000).

Figure 5 shows the evolution of the crosstalk matrix in equation 11 as more synthetic experiments are imaged and stacked, and highlights the increasing signal-to-noise ratio described above. The main diagonal is a perfect spike and indicates that we are not constraining the range of spatial components in the image. Stacking the images obtained with different realizations of random delays, we decrease the energy of the out-of-diagonal terms and, consequently, the signal-to-noise ratio increases linearly with the number of random delay realizations (Romero et al., 2000). The image obtained by random shot-encoding approaches the shot-profile migration result as $M \to \infty$.

2. 3 Mixed shot-encoding migration

The observations in the previous sections lead to the cartoon in Figure 2. In the space defined by crosstalk and spatial bandwidth, we can recognize plane-wave migration as one extremum (low crosstalk and low bandwidth) and random shot-encoding as the other extremum (high crosstalk as well as high spatial bandwidth). The cartoon corresponds to a slice at constant computational cost, which is the third axis in this abstract space. We assume a constant computational cost in order to consistently compare the different approaches. We can imagine moving in the space described by crosstalk and spatial bandwidth by combining the previously presented encodings. Our new approach aims to simultaneously reduce the crosstalk and increase spatial bandwidth as we move toward the center of the crosstalk-bandwidth plane. Of course, the ideal goal is to move towards the upper-right corner (high bandwidth and low crosstalk), and the combination of linear and random shot-encoding is a proxy for this result. Indeed, if we are able to control the artifacts in the image and reduce the crosstalk power, we can filter them out in post processing, thus preserving the structural information in the image and moving toward the shot-record migration result at a lower cost.

The combination of linear and random shot-encoding involves dithering the plane waves with a random perturbation (Figure 3(c)). The expected result is the reduction of crosstalk (because of the side lobes that characterize the crosstalk term for L-SEM) and an increase in spatial bandwidth (given the spikiness of the crosstalk term for R-SEM). In Figure 6, we show the crosstalk matrix for the new mixed shot-encoding scheme:

$$\begin{aligned} W_{kl} &= \sum_\theta e^{i\omega[\mathbf{p}_\theta(\mathbf{x}_l - \mathbf{x}_k) + (t_l^\theta - t_k^\theta)]} \\ &= M\delta_{kl} + (1 - \delta_{kl}) \sum_\theta e^{i\omega[\mathbf{p}_\theta \Delta\mathbf{x}_{kl} + \Delta t_{kl}^\theta]}; \end{aligned} \quad (12)$$

we can observe the behavior in-between linear and random shot-encoding. The crosstalk term partially preserves the char-

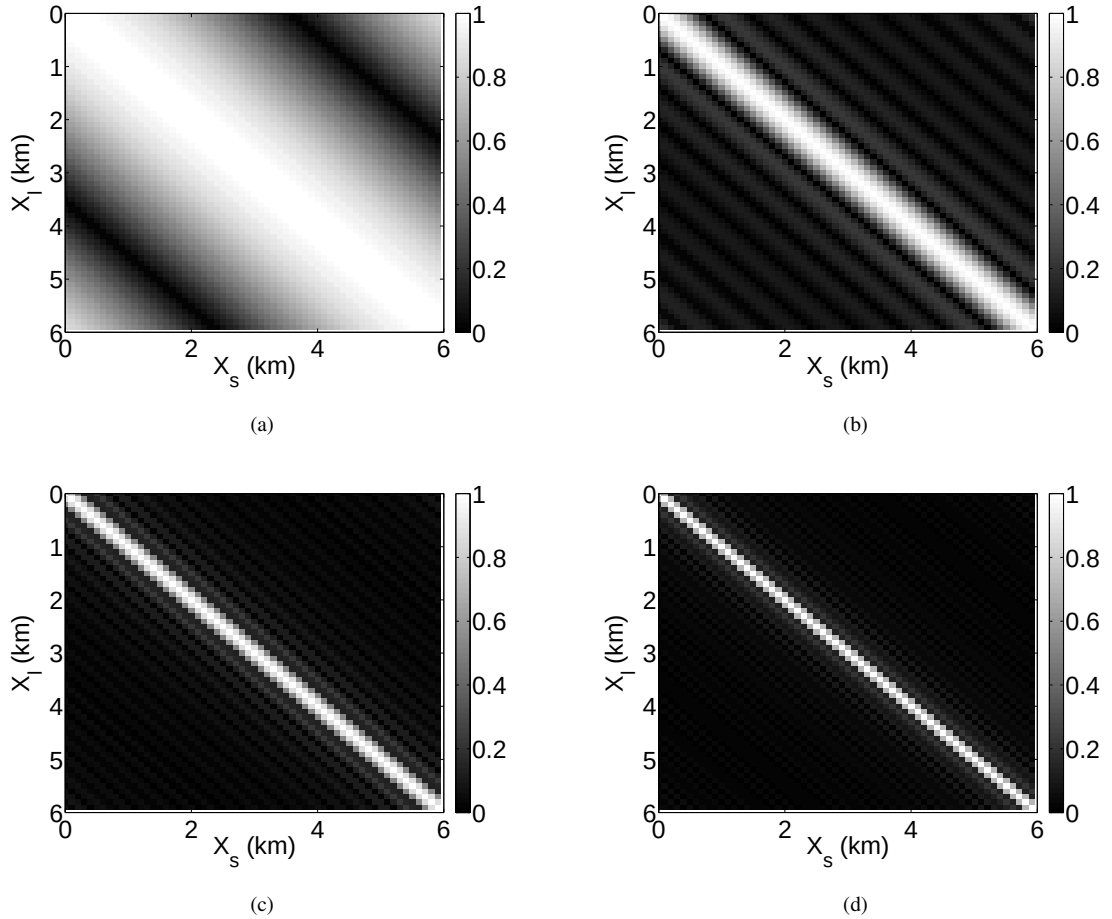


Figure 4. L-SEM crosstalk matrix VS number of plane waves for a single temporal frequency ω: (a) 2, (b) 10, (c) 20, and (d) 30. Increasing the number of plane waves, we sharpen the main diagonal of the crosstalk matrix and better approximate the identity, i.e., we tend toward the shot-record migration result.

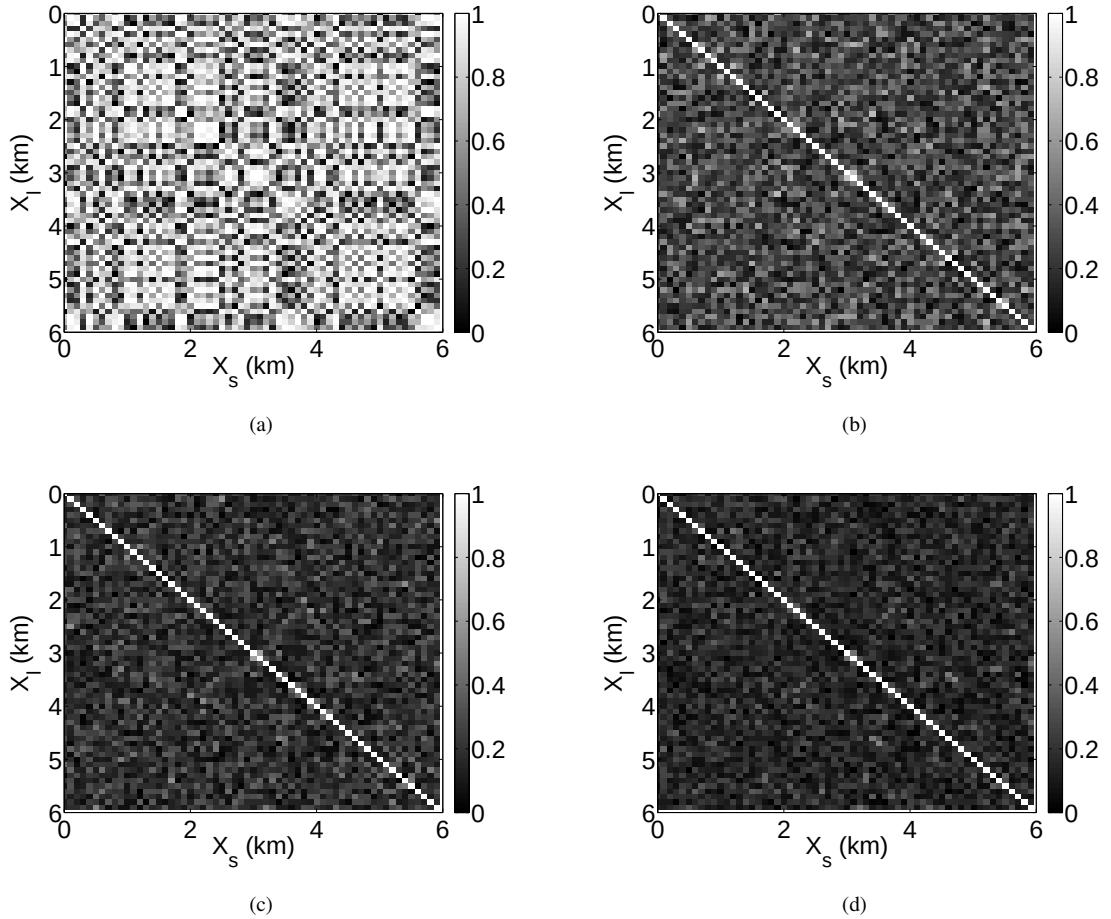


Figure 5. R-SEM crosstalk matrix VS number of synthetic experiments: (a) 2, (b) 10, (c) 20, and (d) 30. The more random-delay realization we consider, the better we approximate the artifact random process. Since the artifacts are zero mean and the stack of a number of experiments is an estimate of the expected value of the process, we are able to remove the crosstalk noise by stacking the images obtained from different random-delay encodings.

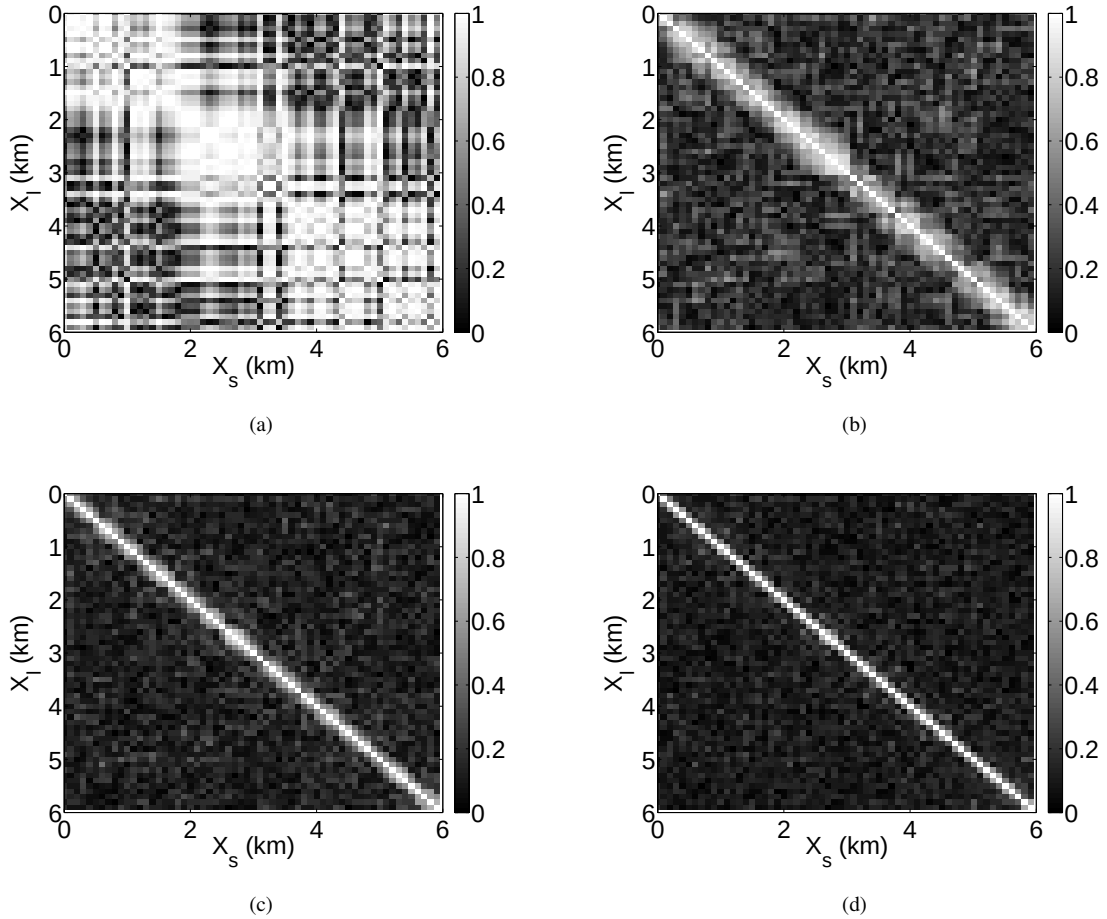
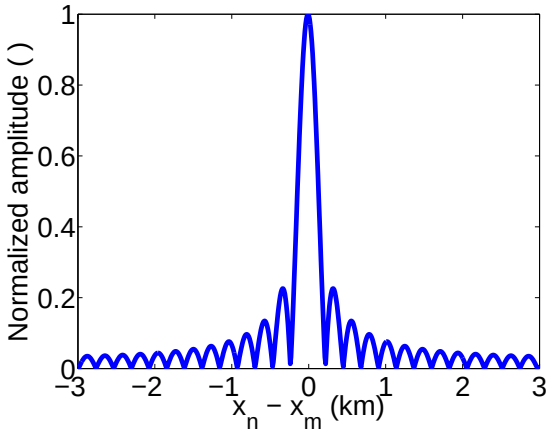
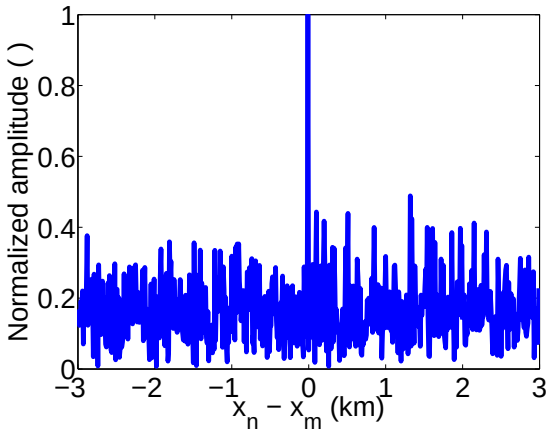


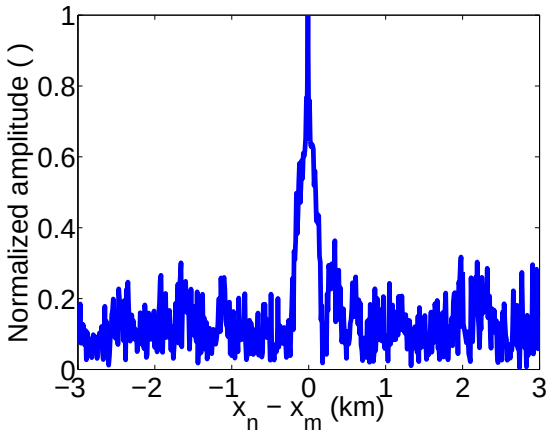
Figure 6. M-SEM crosstalk matrix VS number of experiments: (a) 2, (b) 10, (c) 20, and (d) 30. Combining L-SEM and R-SEM, we obtain a crosstalk matrix characterized by a hybrid behavior. In the panels, we observe the L-SEM convergence footprint and the random fluctuations due to the wavefront dithering. The dithering is particularly effective in sharpening the main diagonal of the crosstalk matrix.



(a)

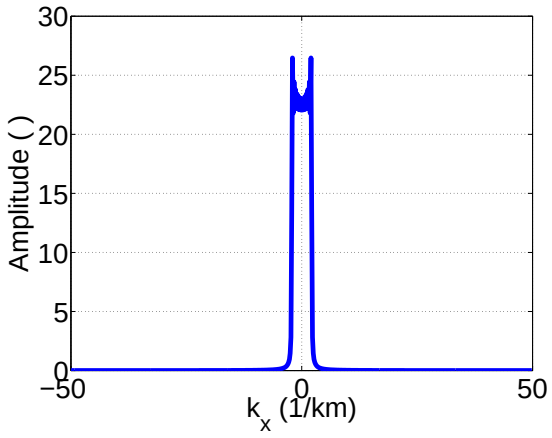


(b)

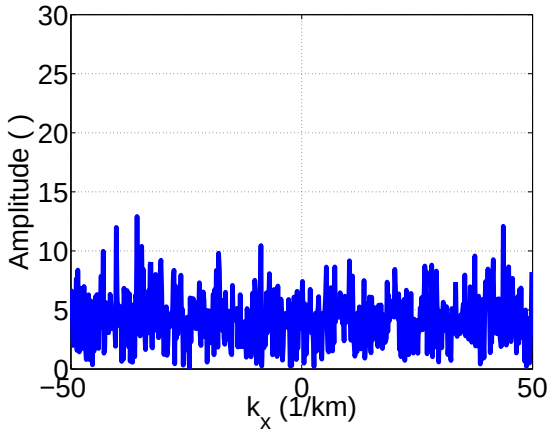


(c)

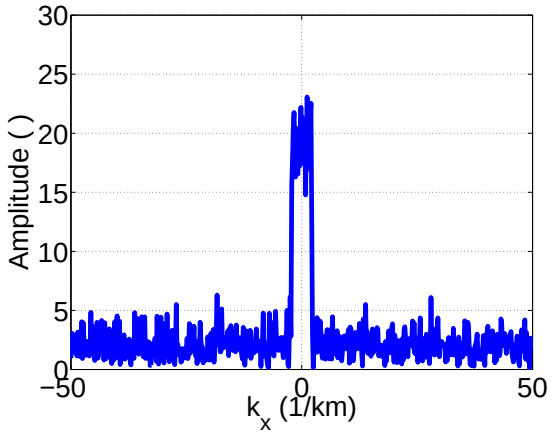
Figure 7. Slices of the crosstalk panel for 50 synthetic experiments: (a) L-SEM, (b) R-SEM, and (c) M-SEM. They represent the coupling of the wavefields of different shots as a function of the distance between the shots.



(a)



(b)



(c)

Figure 8. Plane-wave components considered in the imaging procedure for: (a) L-SEM, (b) R-SEM and (c) M-SEM. L-SEM migrates all the plane-wave components in a limited range with the same weight; R-SEM images all the plane-wave components with uneven amplitudes; M-SEM gives more weight to the dithered plane waves but images all components.

acteristic trend of linear shot-encoding with respect to the side lobes while the dithering destroys the coherency of the side lobes and allows for a spikier main lobe.

Restricting our attention to a single column (row) of the panels in Figures 4-6 , we can better appreciate the behavior with respect to spatial bandwidth and artifacts of L-SEM, R-SEM and M-SEM, respectively. Figure 7(a) shows the absolute value of a column (row) of the crosstalk term in the case of L-SEM and 50 plane waves. Note the main lobe and decaying side lobes. Intuitively, we can think of the width of the main lobe as an indicator of the achieved spatial bandwidth, since it describes the coupling between neighboring shots. The amplitude of the side lobes determines the strength of the artifacts in the image. In this case, we expect a loss in spatial resolution but small artifacts in the final image. We verify these considerations in the result section. For R-SEM (Figures 7(b)) we observe a spike at $\mathbf{x}_n - \mathbf{x}_m = 0$, i.e., when the source and receiver wavefields belong to the same shot, over a random noise floor, which represents the interference between different shots. The spike indicates that we are not trading off the bandwidth of the image; the nonzero terms for $\mathbf{x}_n \neq \mathbf{x}_m$ determines the artifacts. M-SEM (Figure 7(c)) presents a behavior in between L-SEM and R-SEM. The spike for the crosscorrelation of wavefields belonging to the same shots ($\mathbf{x}_n - \mathbf{x}_m = 0$) is produced by the dithering, while the linear trend reduces the out-of-diagonal term of the crosstalk matrices.

Figure 8 shows us how the different encodings take into account the plane-wave components. In Figure 8(a), we see that plane-wave migration is constrained by the range of synthesized ray parameters. At the other extremum, R-SEM images all the components but the equalization among them is missing. In Figure 8(b), the "non-flatness" of the spectrum is the counterpart of the artifacts due to crosstalk in the image. Finally, in Figure 8(c), we observe how M-SEM images all the spatial components giving greater weight to those related to the ray parameters of the plane-waves that have been dithered. Again the "non-flatness" reflects the presence of artifacts in the image. Nonetheless, the distortion is less pronounced than for R-SEM.

2. 4 Example of a point scatterer in constant background

We illustrate the features highlighted in the previous sections with a simple exercise that images a point scatterer in a constant velocity background. We compare the results obtained by stacking 50 images constructed with linear, random and mixed shot-encoding (Figure 9). In all three cases, the maximum delay applied to wave-fields is the same and is equal to 1 s. For imaging algorithms implemented in the time domain, like reverse-time migration, the fixed maximum delay ensures that all migrations have same cost, regardless of the encoding type.

Notice the lower focus of the image obtained by L-SEM (Figure 9(a)). The point is spread in the horizontal direction because we have not considered plane waves with high values of θ in the imaging process, i.e., with high ray parameter $\mathbf{p}$. On the other hand, the image is clean because the crosstalk decreases quickly with the distance $(\mathbf{x}_k - \mathbf{x}_l)$. The data synthesized for plane-wave migration contain the minimum number of events: the response to an incident plane-wave contains the same number of reflection events in the shot-profile data. Because of this, the undesired crosscorrelations between wavefields from different experiments, and then the crosstalk, are minimized. R-SEM (Figure 9(b)) represents the other extremum in the trade-off between crosstalk and spatial bandwidth. In this case, a wider range of the spatial components is imaged but crosstalk noise is present in the image, as well. The synthetic experiments contain more events than the single shot-profile data, and then for a encoded image the crosstalk is maximized. The stack of the different experiments is effective for this simple model but the result rapidly worsens with increasing complexity of the subsurface. Figure 9(c) shows the image obtained by M-SEM. We can observe a spatial resolution that is closer to R-SEM but has fewer artifacts. The amplitude spectra of the stacked images in Figure 10 highlight the smaller spatial bandwidth of L-SEM with respect to both R-SEM and M-SEM. Nonetheless, they show the distortion of the spectrum, i.e., the artifacts in the image. Notice the smaller distortion in the case of M-SEM compared to R-SEM (Figure 10(c) and 10(b), respectively).

2. 5 Denoising and image enhancing

Because M-SEM preserves the full-bandwidth information but the image is contaminated with noise, we can consider removing that noise in post-processing by applying a suitable denoising algorithm. The criterion for choosing among different denoising procedures is the preservation of the geologic features in the image. We test two denoising schemes: the first is based on seislet transform (Fomel, 2006), the second is a nonlinear structure-enhancing algorithm (Liu et al., 2009) based on plane-wave destruction filters (Fomel, 2002).

2. 5.1 Denoising using the seislet transform

The seislet transform (Fomel, 2006) is a wavelet-like transform that decomposes the signal into its components at different scales according to the local dip. This transform is very effective in removing uncorrelated noise from a seismic image and preserving the structures that characterize the image itself. After the seislet decomposition, we reconstruct the image using all but the smallest scale coefficients in order to eliminate the incoherent part of the signal. This approach is based on the assumption that the crosstalk is both incoherent and weaker than the desired signal. Unfortunately, this is not always the case.

2. 5.2 Denoising using nonlinear structure-enhancing filters

As an alternative denoising procedure, we test the structure-enhancing algorithm proposed by Liu et al. (2009). The non-

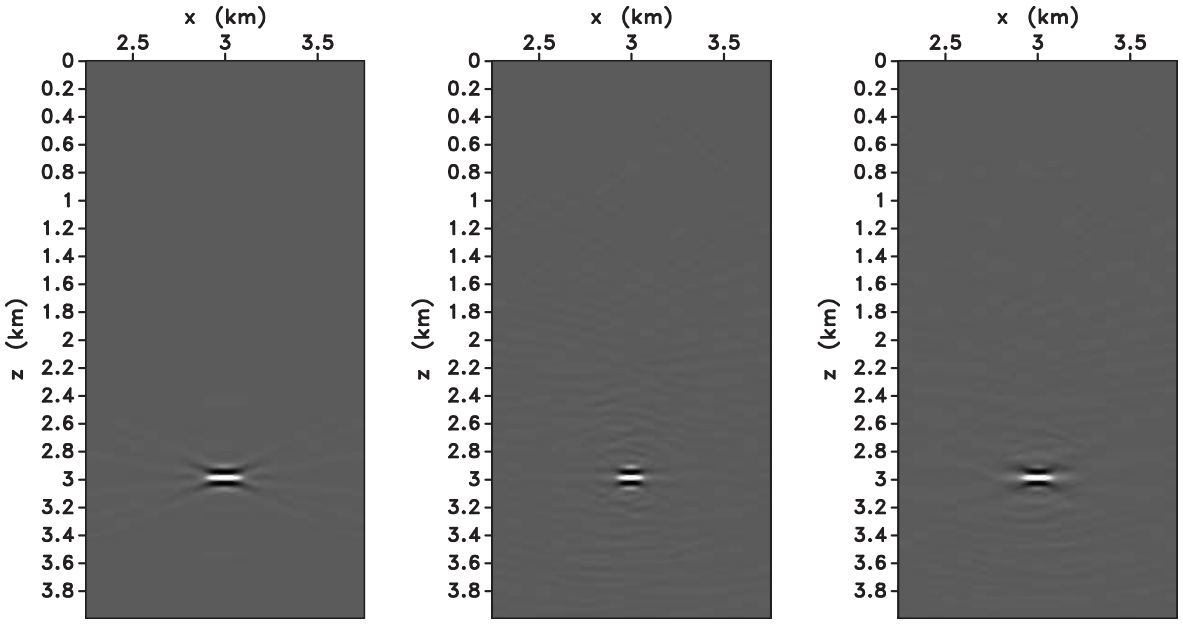


Figure 9. Point scatterer in a constant medium: (a) L-SEM, (b) R-SEM, and (c) M-SEM. Observe the horizontal spreading in L-SEM; the limitation in spatial components reduces the spatial bandwidth of the image. R-SEM produces a sharper image but creates artifacts; M-SEM provides an full-bandwidth image and controls the crosstalk with respect to R-SEM.

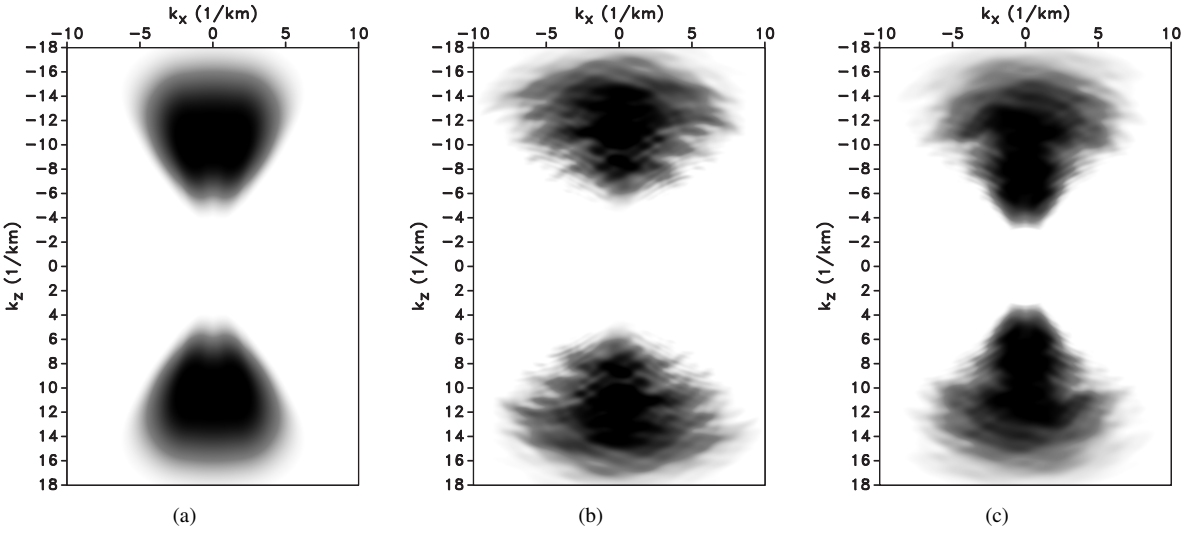


Figure 10. Spatial spectra of the images obtained by (a) L-SEM, (b) R-SEM, and (c) M-SEM. R-SEM distorts the spectrum of the image but recovers all the spatial components; on the contrary, L-SEM is constrained by the plane waves synthesized. M-SEM reduces the distortion of the spectrum and images a wider range of spatial components.

linear structure-enhancing algorithm operates on a extended cube, which is created by plane-wave prediction from a starting image; then, filtering acts across the prediction axis by selecting point-wise the median value of the predicted images. In our case, the starting image is the stack of the mixed shot-encoding synthetic experiments.

3 SIGSBEE EXAMPLE

In this section, we illustrate the technique in a more realistic case by imaging the Sigsbee dataset. In the previous section, we have analyzed the mixed shot-encoding algorithm in the case of a point scatterer in a homogeneous velocity model. We point out the reduction in crosstalk, with respect to random shot-encoding, and the increase in spatial bandwidth with regard to linear shot-encoding migration. Here, we verify those results in a general case.

From the simple example of a point scatterer, we know that the crosstalk is attenuated but not completely suppressed. Nonetheless, if we are able to control the noise during the imaging step, we can apply any denoising algorithm for cleaning up the image from residual artifacts. Results are discussed at the end of the section.

The crosstalk in the final image is heavily dependent on the complexity of the model. In a complex, heterogeneous velocity model, plane waves are distorted and the phase relations that define W_{kl} break down as soon as inhomogeneities are encountered. On the other hand, R-SEM is more robust against this problem since there is no phase coherency to be preserved.

Let us now consider the complex Sigsbee model. Fixed the computational cost, we consider 50 shots for SRM and 50 different experiments that combine all 500 shots of the survey for the three encoding strategies. The migration algorithm used is downward continuation and the maximum delay applied to a single shot is ± 2 s.

Figure 11 shows the image obtained by migrating 50 shots separately (standard shot-record migration). The shot-record migration image represents our benchmark with respect to cost and image quality.

In order to compare the different encoding strategies, we look at the two parts of the image indicated by the boxes in Figure 11. The areas of particular interest are above the salt body, where we want to clearly resolve the stratigraphic sequence, and below the salt body, where the poor illumination and the complexity of the overburden make imaging challenging. In both areas, the signal-to-crosstalk ratio have to be high and the reflectors have to be interpretable despite the interference produced by the simultaneous migration of several shots; furthermore, the spatial spectrum of the image must be accurately recovered in order not to have artifacts in the final result. Indeed, the lack of illumination (mainly due to the salt body) weakens the signal-to-noise ratio for every encoding scheme, and in particular for R-SEM (see Figure 12(b) below the salt body at $z = 5.5$ km). Moreover, because of the heterogeneity of the velocity model in the overburden, synthetic plane-waves are severely distorted and L-SEM becomes inaccurate (see Figure 12(a); at $x = 10$ km the faults are not imaged).

In Figure 12(a) the illumination footprint of L-SEM is easily observable. By imaging only a limited range of plane-wave components, we obtain an illumination pattern which differs from the correct one that would have resulted from shot-record migration. Moreover, not all faults are imaged because of the constraints on the range of migrated plane-wave components ($x = 10$ km). Nonetheless, note the absence of residual diffractions below the salt body ($z = 5$ km) due to the undersampling of the shot domain, previously observed in the shot-record migration image.

The illumination pattern for R-SEM (Figure 12(b)) and M-SEM (Figure 12(c)) is consistent with SRM, but artifacts are introduced by the encoding procedure. In both cases, we are able to image the full spatial bandwidth information of the image but strong crosstalk contaminates the R-SEM result, especially in poorly illuminated areas and near the salt boundaries. M-SEM produces weaker crosstalk both above and below the salt bodies; especially in poorly illuminated areas, M-SEM supplies an interpretable image (compare Figure 12(c) and Figure 12(b) at $z = 5.5$ km).

The close-ups on the selected areas confirm the above considerations. Figure 13(b) is has poor spatial resolution with respect to 13(a): note the spread point diffractor at $z = 5$ km. The number of plane-wave components used is clearly insufficient for the complexity of the Sigsbee model; thus, the information about the faults in the image is largely lost ($x = 10$). R-SEM (Figure 13(c)) recovers a more complete image where the illumination is high but loses coherency under the salt body because of the overwhelming level of crosstalk. In areas of poor illumination, the image is uninterpretable. On the other hand, Figure 13(d) shows that M-SEM recovers most of the image spatial bandwidth (in contrast to L-SEM) and increases the signal-to-crosstalk (in contrast to R-SEM) below the salt body.

The image above the salt body warrants a separate discussion. Looking at the SRM image (Figure 14(a)), we note that L-SEM (Figure 14(b)) produces a clearer image (no residual diffractions) but the amplitudes in the image are also lower. This is likely related to the limitation imposed on the range of plane-wave components that have been imaged. Figure 14(c) shows the image obtained by R-SEM. All the information about the reflectors is preserved and the incoherence of the encoding delays, together with the strong illumination of the area, enable a better control of the artifacts, which appear to be incoherent and uncorrelated with the signal. M-SEM slightly improves the amplitudes of the reflection but also introduces a certain amount of correlated noise in the image (Figure 14(d)). Nonetheless, no information is lost with respect to the SRM (Figure 14(a)).

3. 0.3 Effects of dithering on crosstalk

The previous examples of imaging with mixed shot-encoding involve a 0.5% dithering of the initial plane-wave. It is of interest to look at the effects of the amount of dithering on the quality of the final image.

Intuitively, we obtain the L-SEM image by reducing the

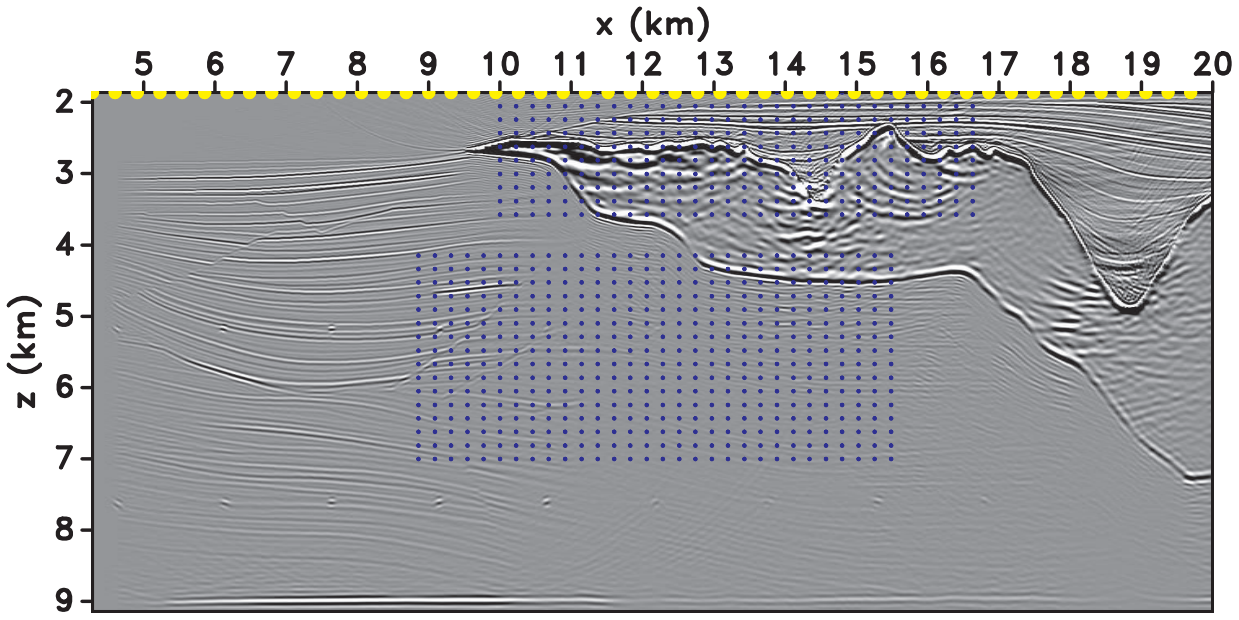


Figure 11. SRM of the Sigsbee dataset; the image is the stack of 50 shot-record migrations. The boxes highlight the areas we analyze in detail in Figures 13-14.

dithering, but relation between the amount of perturbation and the increase in the spatial bandwidth of the image cannot be easily evaluated. In Figure 15(a), we show the standard plane-wave migration image. Figure 15(b) is the result previously discussed (Figure 13(d)); note the considerable increase in spatial detail achieved with respect to plane-wave migration. The faults in the image are now interpretable and the point scatterers are better reconstructed. The illumination pattern is controlled by the main plane-wave components and closely resembles the illumination pattern in Figure 15(a). Increasing the dithering (1% and 10% in Figures 15(c)-15(d), respectively), we equalize the illumination of the image and recover greater spatial detail but, at the same time, we introduce stronger distortion, especially in the subsalt area. We conclude that a relatively small amount of dithering is necessary for sensibly increasing the spatial bandwidth of the final result. Nonetheless, it is difficult to quantify the optimum dithering, again because of the model-dependence of the problem. Given a dataset, we could estimate it *a posteriori*, crossing different image-quality indicators (spatial spectrum, image entropy, etc.) but this strategy would reduce the cost-effectiveness of M-SEM.

3. 0.4 Denoising and image enhancing

Mixed shot-encoding is more robust against crosstalk than R-SEM and it supplies a full spatial bandwidth image; nonetheless, the final image is not completely free from crosstalk. Let us now discuss the effectiveness of the postprocessing denoising algorithm against this kind of noise. Denoising is applied to an image constructed by dithering the planar wavefront with a random perturbation ranging within 0.5% of the maximum delay.

For M-SEM, the seislet denoising is effective above the salt (Figure 16(b)), but it does not improve the image quality below the salt (Figure 17(b)) because of the relatively good quality of the starting image and poor illumination of the area. The latter impacts the signal-to-crosstalk ratio and makes signal and artifacts not easily separable in the seislet domain. Overall, seislet transform is not effective in increasing the quality of the M-SEM result.

In Figure 16(c) we observe that, above the salt, the structure-enhancing algorithm is actually effective in cleaning the image and preserving the reflectors. Below the salt the situation is different; M-SEM already produces weaker artifacts and the nonlinear filtering is able to partially enhance the sediments and reflectors in this poorly illuminated area (Figure 17(c)). Moreover, the procedure is highly sensitive to amplitudes and tends to sharpen amplitude contrasts. This is a positive feature for highlighting faults but it can also lead to misleading amplitude behavior in poorly illuminated areas. In conclusion, the denoising procedure contributes marginal improvements to the initial M-SEM image.

4 DISCUSSION

The examples presented in the previous sections show the robustness of M-SEM against artifacts produced by crosstalk between different shots. A single point scatterer in a homogeneous velocity medium is imaged with more spatial components with respect to L-SEM and, at the same time, the distortion of its spatial spectrum is less significant with respect

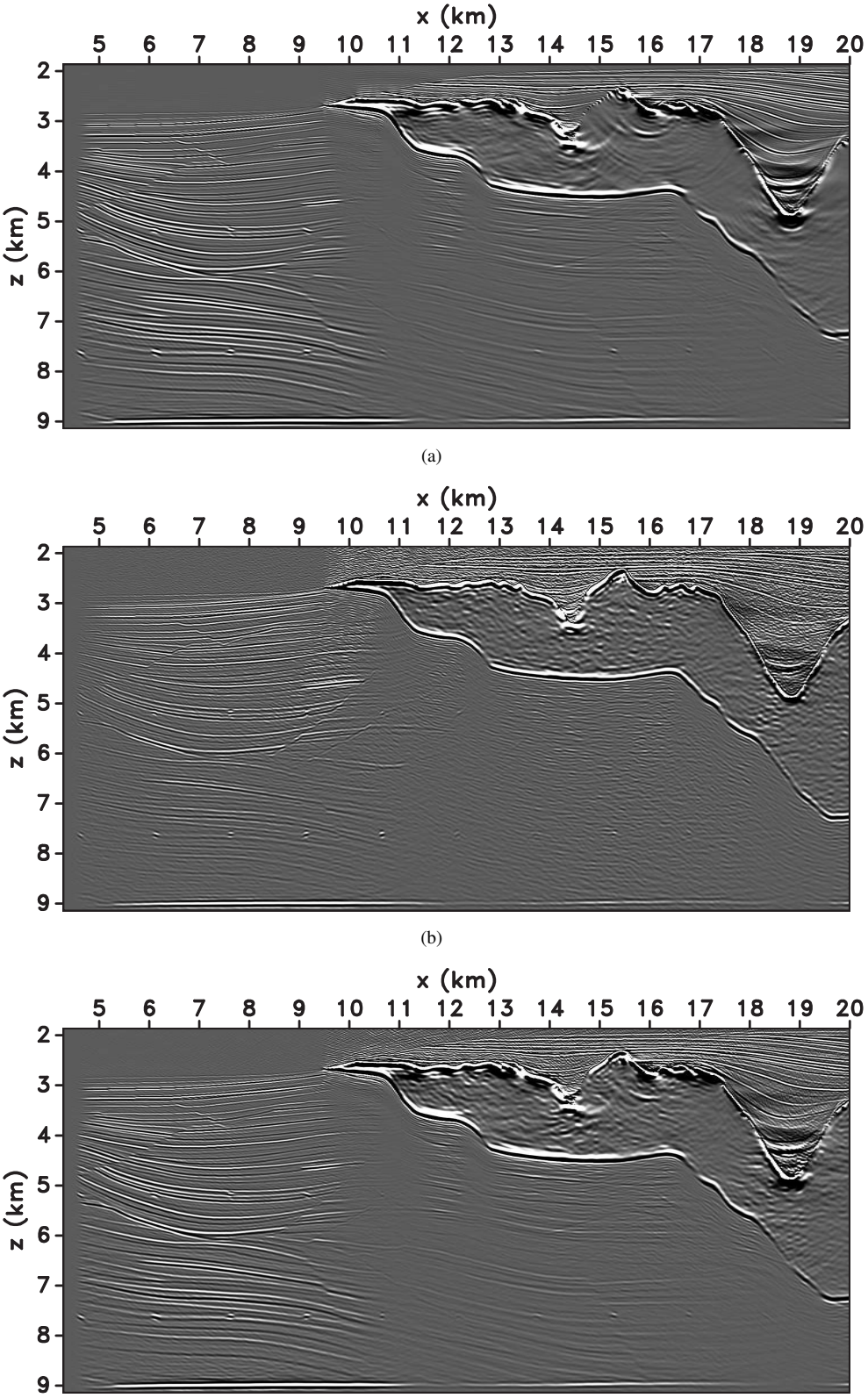


Figure 12. Sigsbee dataset migrated using different encoding schemes: (a) L-SEM, (b) R-SEM, and (c) M-SEM. 50 synthetic experiments have been used for each encoding method.

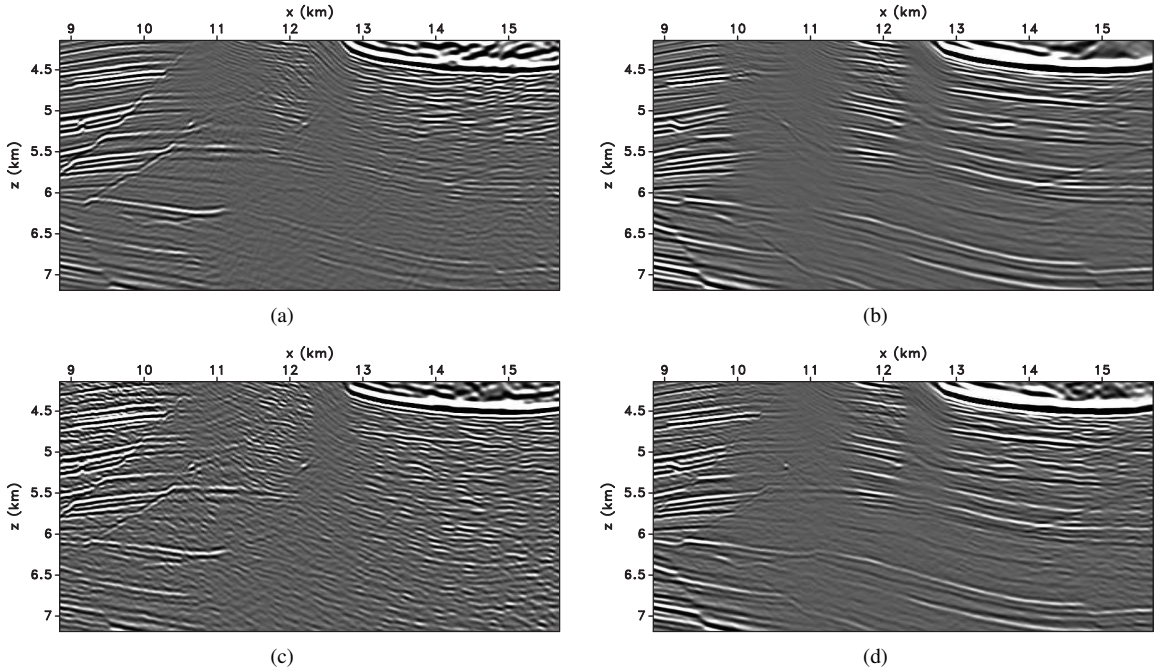


Figure 13. Image detail below the salt body: (a) SRM, (b) L-SEM, (c) R-SEM, and (d) M-SEM. The undersampling of the shot dimension is particularly important below the salt bodies and results in residual diffraction events that distort the image. L-SEM images correctly flat events but loses the fault information and the point diffractors. R-SEM reconstructs the complete spatial information but introduces crosstalk noise below the salt, where illumination is poor. M-SEM obtains a clearer image, with respect to R-SEM, better images the faults and the point diffractors, compared with L-SEM, and achieves an interpretable image below the salt, differently from the undersampled SRM.

to R-SEM. Hence, with M-SEM we span the domain in between the two extremal strategies represented by L-SEM and R-SEM.

This result gives us confidence about the success of M-SEM when applied to imaging in complex velocity models. Indeed, in a heterogeneous velocity field, L-SEM also produces important artifacts caused by the distortion of the planar wavefront and triplications of the wavefield. The delay incoherence, typical for R-SEM, is useful in recovering full bandwidth and effective in destroying the coherence of the artifacts in the migrated image.

The effectiveness of the encoding is directly related to the behavior of the crosstalk matrix. In order to be completely free from artifacts, the sequence of crosstalk matrices must tend to the identity. The encoding problem can then be rephrased in terms of approximation to the identity. In this section, we analyze in greater detail why M-SEM is more effective in imaging in complex velocity models.

The crosstalk term W_{kl} for the three encodings presented in the previous sections is

$$W_{kl}^{L} = \sum_{\theta} e^{i\omega \mathbf{p}_\theta (\mathbf{x}_l - \mathbf{x}_k)} \ , \tag{13}$$

$$W_{kl}^{R} = \sum_{\theta} e^{i\omega [t_l^\theta - t_k^\theta]} \ , \tag{14}$$

$$W_{kl}^{M} = \sum_{\theta} e^{i\omega \left[\mathbf{p}_\theta (\mathbf{x}_l - \mathbf{x}_k) + (t_l^\theta - t_k^\theta)\right]} \ , \tag{15}$$

for L-SEM, R-SEM and M-SEM, respectively. In the case of L-SEM and R-SEM, equations 13 and 14 actually approximate the identity but from very different points of view. In the first case, the completeness of the Fourier basis functions is invoked; in the second case, the uncorrelation of delays and artifacts, in the data and the final image, respectively, yields the result. W_{kl}^{L} converges slowly and smoothly toward the identity operator but does not introduce strong artifacts; on the other hand, W_{kl}^{R} converges toward the identity matrix by attenuating the random out-of-diagonal terms. The out-of-diagonal terms contribute strong crosstalk, which is iteratively reduced by stacking different synthetic experiments obtained from different random delay realizations.

The crosstalk matrix for M-SEM in equation 15 can be rewritten as follows:

$$W_{kl}^{M} = \sum_{\theta} e^{i\omega \left[\mathbf{p}_\theta \Delta \mathbf{x}_{kl} + \Delta t_{kl}^\theta\right]}; \tag{16}$$

separating the terms for $k = l$ and collecting $\Delta \mathbf{x}_{kl}$ in the exponent, yields

$$W_{kl}^{M} = M\delta_{kl} + (1 - \delta_{kl}) \sum_{\theta} e^{i\omega \left[\left(\mathbf{p}_\theta + \frac{\Delta t_{kl}^\theta}{\Delta \mathbf{x}_{kl}}\right) \Delta \mathbf{x}_{kl}\right]}. \tag{17}$$

The ratio $\frac{\Delta t_{kl}^\theta}{\Delta \mathbf{x}_{kl}}$ has the dimensions of a ray parameter

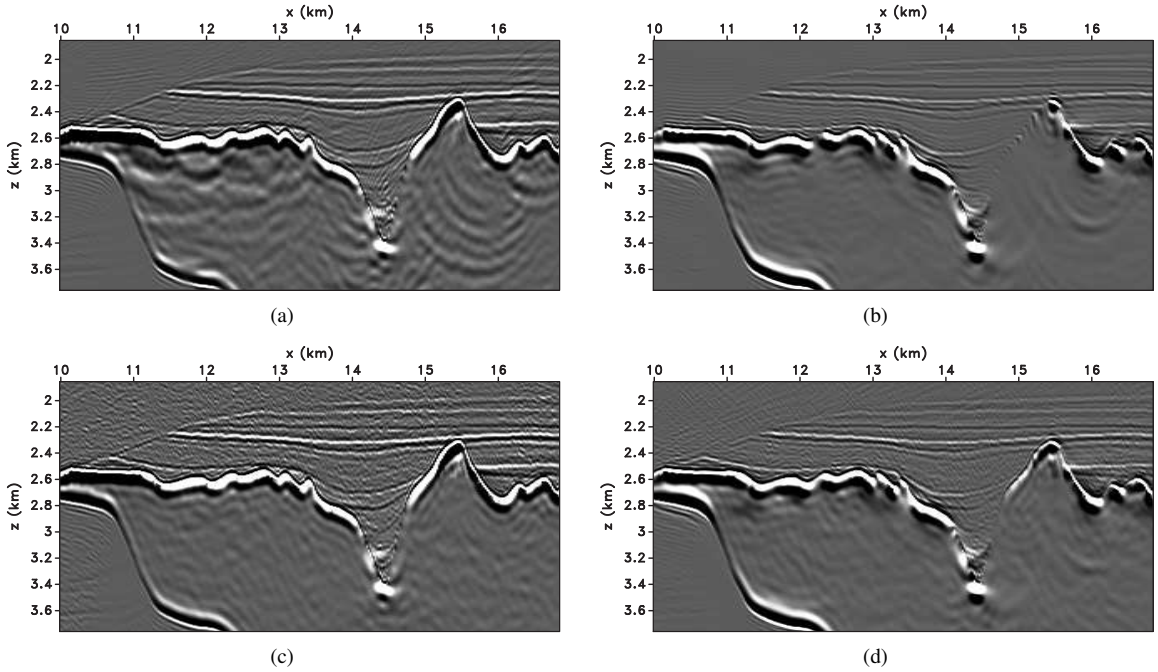


Figure 14. Image detail above the salt body: (a) SRM, (b) L-SEM, (c) R-SEM, and (d) M-SEM. The SRM presents correlated noise due to the undersampling of the shot dimension. L-SEM is able to very well recover nearly horizontal events, but the top of salt is smoothed out and the steep flank of salt canyon are not well imaged. R-SEM introduces random-like noise but images correctly the structures and the rugose top of the salt. M-SEM reduces the crosstalk, images correctly the almost horizontal events and obtains a better image of the top of the salt.

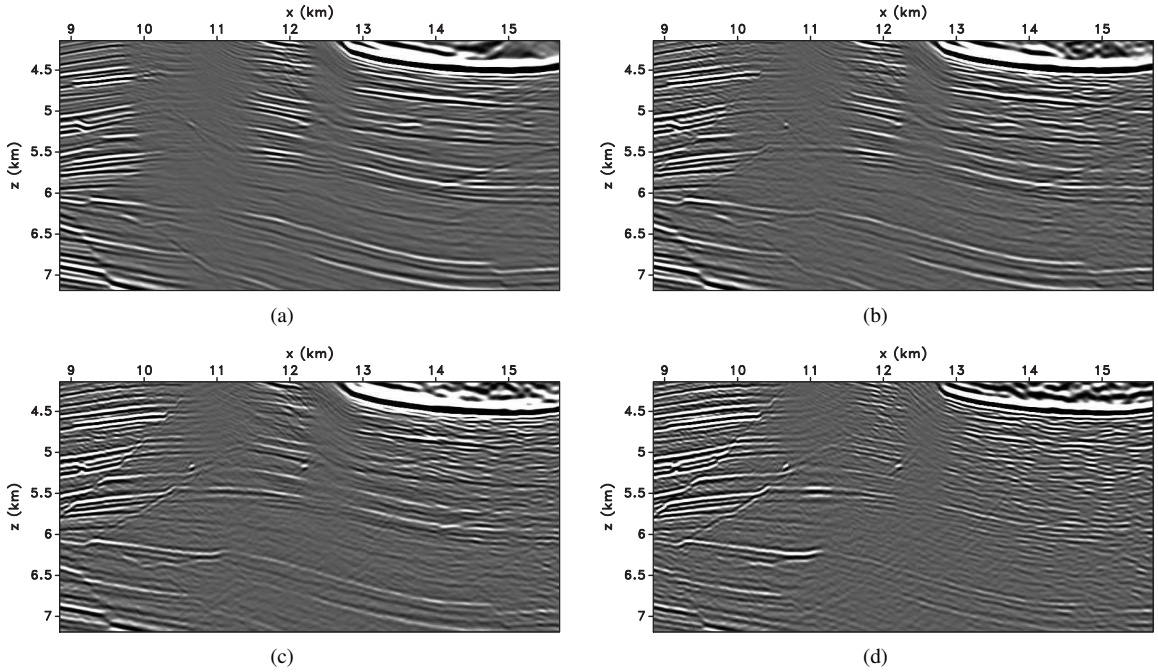


Figure 15. Effects of the amount of dithering on the image: (a) L-SEM, (b) 0.5%, (c) 1% and (d) 10% of the maximum delay. We observe the smooth increase of both spatial detail and crosstalk noise, especially subsalt.

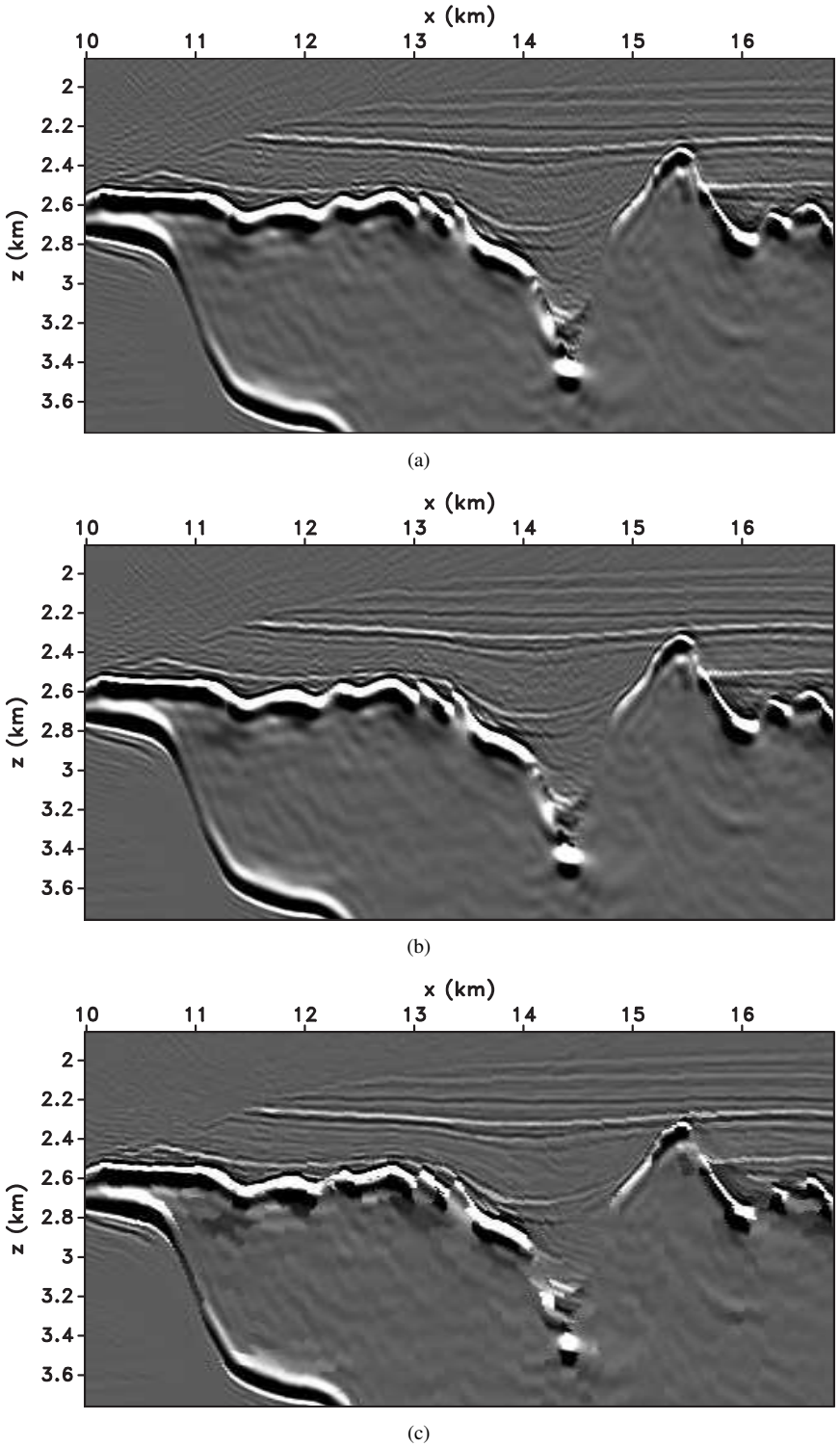
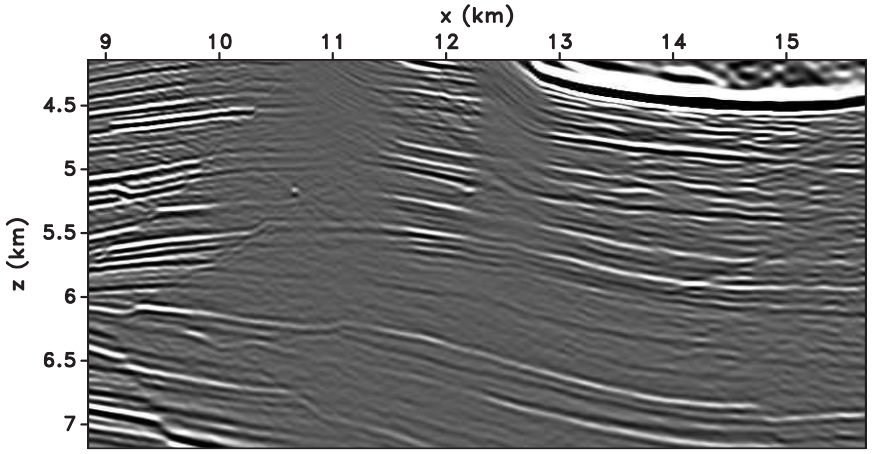
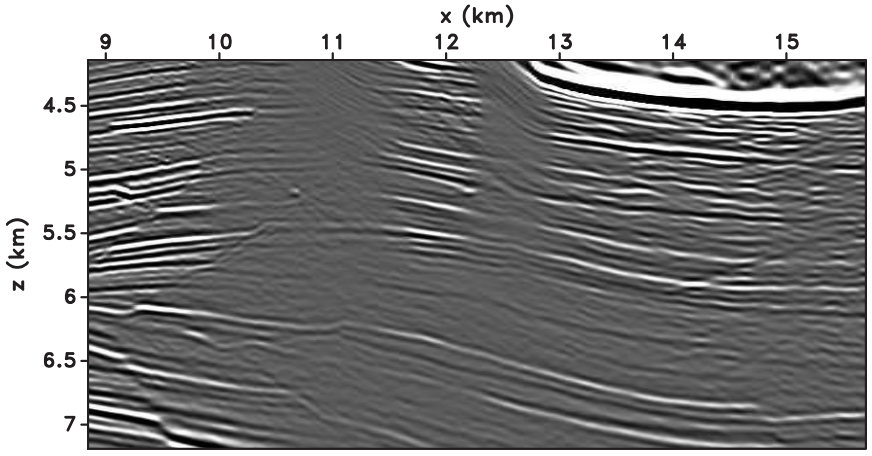


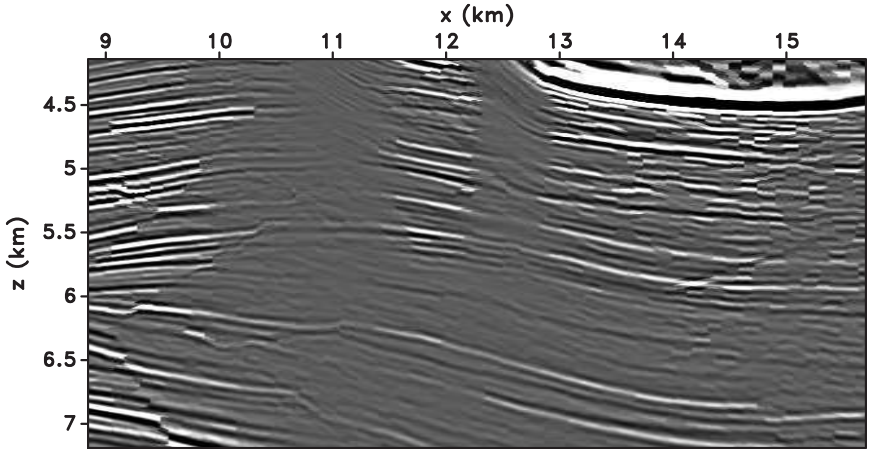
Figure 16. Results after denoising. (a) M-SEM image detail above the salt body. Both (b) seislet transform denoising and (c) nonlinear structure enhancing algorithm are effective in removing incoherent noise where the dip field of the image is slowly varying. If conflicting dips are present, the image is distorted; observe the flank of the salt canyon.



(a)



(b)



(c)

Figure 17. Results after denoising. (a) M-SEM image detail below the salt body. In poorly illuminated areas, crosstalk is hardly distinguishable from the signal. (b) seislet transform denoising removes high scale noise but does not affect the image below the salt body; (c) nonlinear structure enhancing algorithm boosts amplitude differences, sharpening faults, but cancels the point diffractors.

and can be viewed as a perturbation of the the plane-wave ray parameter $\mathbf{p}_\theta$. Note that the perturbation varies spatially since it depends on $\Delta\mathbf{x}_{kl}$; the non-stationary nature of the ratio $\frac{\Delta t^\theta_{kl}}{\Delta\mathbf{x}_{kl}}$ allows us to gain spatial resolution with respect to standard plane-wave migration, since a greater number of "equivalent" spatial components $p^{eq}_\theta = \mathbf{p}_\theta + \frac{\Delta t^\theta_{kl}}{\Delta\mathbf{x}_{kl}}$ is imaged; however, it also introduces a disturbance in the convergence of the crosstalk matrix toward the identity operator, i.e., random-like artifacts in the final image.

Let us consider two limit cases. If $\Delta\mathbf{x}_{kl}$ is "small", i.e., if we are close to one particular shot location, we have

$$p^{eq}_\theta = \mathbf{p}_\theta + \frac{\Delta t^\theta_{kl}}{\Delta\mathbf{x}_{kl}} \longrightarrow \frac{\Delta t^\theta_{kl}}{\Delta\mathbf{x}_{kl}}; \tag{18}$$

on the other hand, if $\Delta\mathbf{x}_{kl}$ is "large", i.e., if we are considering the mutual influence of two distant shots, we have

$$p^{eq}_\theta = \mathbf{p}_\theta + \frac{\Delta t^\theta_{kl}}{\Delta\mathbf{x}_{kl}} \longrightarrow \frac{\sin(\alpha\theta)}{v}. \tag{19}$$

Mixed shot-encoding behaves like R-SEM (see equation 18) when we consider neighboring shots, and resembles L-SEM when we look at the effects on a particular shot from more distant ones (see equation 19). This different behavior explains the increase in the spatial resolution (with respect to L-SEM) and the decrease in crosstalk (with respect to R-SEM) that M-SEM is able to achieve.

The analysis of the distribution of the resulting random variable $\frac{\Delta t^\theta_{kl}}{\Delta\mathbf{x}_{kl}}$ is not straightforward; even though we can intuitively understand $\frac{\Delta t^\theta_{kl}}{\Delta\mathbf{x}_{kl}}$ as a random perturbation of a fixed ray parameter p_θ, this perturbation is now spatially-varying along the shot positions because of the term $\Delta\mathbf{x}_{kl}$. This is counterintuitive since we usually associate a ray parameter with a planar wavefront rather than with one that is dithered and not well-defined.

An alternative way of looking at this is to imagine simultaneously migrating a bundle of plane-waves which are randomly taken in the neighborhood of a given p_θ. Actually, M-SEM images more plane-wave components than L-SEM; indeed, it images all the plane-wave components but with uneven relative amplitudes. This conclusion emerges from Figure 8(c): at the surface, M-SEM constructs not only the basis plane waves synthesized in L-SEM, but also plane-wave components outside the limited range of plane-wave migration. The amplitudes are lower and uneven because the additional plane-wave components are obtained in a statistical, rather than deterministic way. Nonetheless, by constraining the random fluctuations of these components, we can reduce the artifacts in the image without limiting the spatial bandwidth. Moreover, if we are able to shape the profile of plane-wave components synthesized at the surface, we can aim to further decrease the crosstalk noise. Considering the L-SEM result as a benchmark for spatial bandwidth and crosstalk, we can evaluate the effects of the amount of dithering on the crosstalk in the final image. We experimentally found that a dithering of 0.5% of the maximum delay is sufficient for spatial details to emerge (compare Figure 15(b) and 15(a)) in areas with poor illumination.

The illumination pattern varies smoothly with the perturbation of the planar wavefront; the amplitudes in the image are distorted with respect to shot-record migration but most of the geometrical and structural information is reliably recovered, although point scatterers and highly corrugated salt boundaries may be smoothed off. In areas with good illumination, if we increase the dithering, we obtain amplitudes that are closer to shot-record migration. On the other hand, in areas with poor illumination, the signal-to-crosstalk ratio is low and reflectors cannot be interpreted (see Figure 15(c) and 15(d) below the salt body).

Fixing the maximum delay, we analyze the different encodings at equal computational cost. M-SEM recovers more spatial components than L-SEM and controls the crosstalk that R-SEM alone would produce. The results on the Sigsbee dataset prove that M-SEM converges faster than both R-SEM and L-SEM toward an image of comparable quality to the one obtained by shot-record migration; 50 synthetic experiments are sufficient for recovering the structural information of the image, and the overall cost of the imaging step is 10% of standard shot-record migration. For the Sigsbee dataset, we consider take-off angles from -14 to 14 degrees, a central frequency $f = 15$ Hz, and a source spacing of 45 m; if the expression in Zhang et al. (2005) for the minimum number of $\mathbf{p}$ components had been used, at least 109 $\mathbf{p}$ components would have been necessary for correctly reconstructing the data. However, we used only 50 dithered plane waves. The dithering allows one to overcome both the limitation in the recoverable spatial bandwidth of the image and the $\mathbf{p}$ component sampling requirements for correctly representing the data. Moreover, since all the shots are encoded in every synthetic experiment, the shot dimension is not undersampled, and no residual diffraction (caused by the aperture limitation of the single shot) is imaged.

5 CONCLUSIONS

We design a hybrid encoding scheme, which we refer to as mixed shot-encoding, that combines the characteristics of linear and random shot-encoding in order to move across the space defined by spatial bandwidth and crosstalk at fixed computational cost. We analyze the behavior of the shot coupling term and test mixed shot-encoding migration on the Sigsbee dataset, verifying the effectiveness of the algorithm. Dithering a planar wavefront, we increase the spatial bandwidth of a single image with respect to linear shot-encoding, and we introduce weaker crosstalk noise with regard to random-shot encoding. We investigate the effects of the amount of dithering on the final image and verify that one can move smoothly for one extremum, L-SEM, to the other extremum, R-SEM. The migrated image results highly sensitive to dithering. Very little perturbation of the wavefront has significant impact on the final image; in particular, the spatial bandwidth increases faster than crosstalk and a relatively small dithering allows one to recover spatial bandwidth without introducing strong artifacts.

We test the effectiveness of postprocessing denoising for enhancing the structural information in the encoded image and for removing the residual crosstalk noise. In general, denoising performs well in areas with good illumination. In areas with poor illumination, the crosstalk is not distinguishable from the signal and denoising becomes ineffective.

There are several possibilities for further research: 1) an accurate analysis of the convergence rate toward shot-record migration will help in estimating the computational cost gain we can achieve through mixed shot-encoding migration; 2) a statistical analysis of the artifacts can provide indications for designing more sophisticated encoding schemes; 3) shaping of the amplitude spectrum of the migrated plane-wave components can further reduce the crosstalk noise in the image; 4) a parallel research direction is the design of denoising strategies based on adaptive subtraction of the artifacts after remodeling of the data. Finally, if the crosstalk is sufficiently under control, i.e., the signal-to-crosstalk ratio is high, mixed shot-encoding migration produces image gathers that can be used for migration velocity analysis.

6 ACKNOWLEDGMENTS

We would like to acknowledge the financial support provided by a research grant from Eni E&P and stimulating technical discussions with Clara Andreoletti and Nicola Bienati. The reproducible numeric examples in this paper use the Madagascar open-source software package freely available from http://www.reproducibility.org.

REFERENCES

Baysal, E., Kosloff, D. D., and Sherwood, J. W. C., 1983, Reverse time migration: Geophysics, **48**, no. 11, 1514–1524.

Berkhout, A. J., Verschuur, D. J., and Blacquière, G., 2009, Seismic imaging with incoherent wavefields: Seismic imaging with incoherent wavefields:, Soc. of Expl. Geophys., 79th Ann. Internat. Mtg., 2894–2898.

Berkhout, A. J., 2008, Changing the mindset in seismic acquisition: The Leading Edge, , no. 27, 924–938.

Claerbout, J. F., 1985, Imaging the earth's interior: , Blackwell Publishing.

Etgen, J., 2005, How many angles do we *really* need for delayed-shot migration?: How many angles do we *really* need for delayed-shot migration?:, Soc. of Expl. Geophys., 75th Ann. Internat. Mtg., 1985–1988.

Fomel, S., 2002, Applications of plane-wave destruction filters: Geophysics, **67**, no. 6, 1946–1960.

Fomel, S., 2006, Towards the seislet transform: Towards the seislet transform:, Soc. of Expl. Geophys., 76th Ann. Internat. Mtg., 2847–2850.

Lailly, P., 1983, The seismic inverse problem as a sequence of before stack migrations *in* Bednar, J. B., Redner, R., Robinson, E., and Weglein, A., Eds., Conference on inverse scattering: Theory and Applications:: SIAM, 206–220.

Liu, F., Hanson, D. W., Whitmore, N. D., Day, R. S., and Stolt, R. H., 2006, Toward a unified analysis for source plane wave migration: Geophysics, **71**, no. 4, S129–S139.

Liu, Y., Fomel, S., and Liu, G., 2009, Nonlinear structure-enhancing filtering using plane-wave prediction: Nonlinear structure-enhancing filtering using plane-wave prediction:, EAGE, Conference and Exhibition.

Morton, S. A., and Ober, C. C., 1998, Faster shot-record migrations using phase encoding: Faster shot-record migrations using phase encoding:, Soc. of Expl. Geophys., 68th Ann. Internat. Mtg, 1131–1134.

Rickett, J., and Sava, P., 2002, Offset and angle-domain common image-point gathers for shot-profile migration: Geophysics, **67**, 883–889.

Romero, L. A., Ghiglia, D. C., Ober, C. C., and Morton, S. A., 2000, Phase encoding of shot records in prestack migration: Geophysics, **65**, no. 02, 426–436.

Sava, P. C., and Fomel, S., 2003, Angle-domain common-image gathers by wavefield continuation methods: Geophysics, **68**, 1065–1074.

Soubaras, R., 2006, Modulated-shot migration: Modulated-shot migration:, Soc. of Expl. Geophys., 76th Ann. Internat. Mtg., 2430–2433.

Stolk, C. C., and de Hoop, M. V., Seismic inverse scattering in the "wave-equation" approach:, Technical Report CWP-417, Center for Wave Phenomena, Colorado School of Mines, 2001.

Stolk, C. C., and Symes, W. W., 2004, Kinematic artifacts in prestack depth migration: Geophysics, **69**, no. 2, 562–575.

Stork, C., and Kapoor, J., 2004, How many P values do you want to migrate for delayed shot wave equation migration?: How many P values do you want to migrate for delayed shot wave equation migration?:, Soc. of Expl. Geophys., 74th Ann. Internat. Mtg., 1041–1044.

Tang, Y., and Biondi, B., 2009, Least-squares migration/inversion of blended data: Least-squares migration/inversion of blended data:, Soc. of Expl. Geophys., 79th Ann. Internat. Mtg., 2859–2863.

Verschuur, D. J., and Berkhout, A. J., 2009, Target-oriented, least-squares imaging of blended data: Target-oriented, least-squares imaging of blended data:, Soc. of Expl. Geophys., 79th Ann. Internat. Mtg., 2889–2893.

Whitmore, N., 1995, An imaging hierarchy for common-angle plane wave seismograms: , PhD thesis, University of Tulsa.

Zhang, Y., Sun, J., C.Notfors, Gray, S. H., Chernis, L., and Young, J., 2005, Delayed-shot 3d depth migration: Geophysics, **70**, no. 5, E21–E28.

Zhang, Y., Sun, J., and Gray, S., 2007, Reverse-time migration: amplitude and implementation issues: Reverse-time migration: amplitude and implementation issues:, Soc. of Expl. Geophys., 77th Ann. Internat. Mtg., 2145–2148.